The Astrophysical Journal, 734:50 (11pp), 2011 June 10 doi:10.1088/0004-637X/734/1/50

A HYBRID SOLAR WIND MODEL OF THE CESE+HLL METHOD WITH A YIN–YANG OVERSET GRID AND AN AMR GRID

Xueshang Feng[1], Shaohua Zhang[1,2], Changqing Xiang[1], Liping Yang[1,2], Chaowei Jiang[1,2], and S. T. Wu[3]
[1] SIGMA Weather Group, State Key Laboratory for Space Weather, Center for Space Science and Applied Research,
Chinese Academy of Sciences, Beijing 100190, China; fengx@spaceweather.ac.cn
[2] College of Earth Sciences, Graduate University of Chinese Academy of Sciences, Beijing 100049, China
[3] Center for Space Plasma and Aeronomic Research, The University of Alabama in Huntsville, AL 35899, USA
Received 2011 February 26; accepted 2011 April 3; published 2011 May 24

ABSTRACT

A hybrid three-dimensional (3D) MHD model for solar wind study is proposed in the present paper with combined grid systems and solvers. The computational domain from the Sun to Earth space is decomposed into the near-Sun and off-Sun domains, which are respectively constructed with a Yin–Yang overset grid system and a Cartesian adaptive mesh refinement (AMR) grid system and coupled with a domain connection interface in the overlapping region between the near-Sun and off-Sun domains. The space-time conservation element and solution element method is used in the near-Sun domain, while the Harten–Lax–Leer method is employed in the off-Sun domain. The Yin–Yang overset grid can avoid well-known singularity and polar grid convergence problems and its body-fitting property helps achieve high-quality resolution near the solar surface. The block structured AMR Cartesian grid can automatically capture far-field plasma flow features, such as heliospheric current sheets and shock waves, and at the same time, it can save significant computational resources compared to the uniformly structured Cartesian grid. A numerical study of the solar wind structure for Carrington rotation 2069 shows that the newly developed hybrid MHD solar wind model successfully produces many realistic features of the background solar wind, in both the solar corona and interplanetary space, by comparisons with multiple solar and interplanetary observations.

Key words: magnetohydrodynamics (MHD) – methods: numerical – solar wind – Sun: heliosphere

1. INTRODUCTION

To discover the solar wind structure from the Sun to Earth and beyond is an important topic in the study of solar-terrestrial physics. It has long been known that the solar wind is one of the primary factors controlling the terrestrial environment and its underlying structures can influence the propagation of solar disturbance and interplanetary transient phenomena such as coronal mass ejections (CMEs) and interplanetary CMEs responsible for geospace storms. In this field also known as space weather, three-dimensional (3D) numerical simulation models are powerful tools and can complement observations. To this end, scientists have developed various numerical models as reviewed by Dryer (2007) and Feng et al. (2011), to which researchers can refer for a comprehensive survey of key scientific problems involved with and a future route to numerical space weather study from the Sun to Earth.

In numerical studies of the solar wind, it is natural to use the spherical shell domain to characterize the computational domain from the inner boundary at the solar surface (1 R_S) to the outer boundary at 1 AU or beyond (Feng et al. 2010). The solar wind and CMEs emanate from the Sun; thus, properly characterizing the solar surface is critically important. The Sun's spherical surface, however, is not consistent with any of the Cartesian or cylinder coordinate grids. The curved inner boundary of the Sun presents a problem when using a generic magnetohydrodynamics (MHD) solver on a Cartesian grid and it is not easy to modify the solver at the boundary while preserving the accuracy of the numerical scheme. The coordinate singularity and the grid convergence near the poles are classic numerical difficulties when one uses spherical coordinates to represent the Sun's spherical shell geometry (Feng et al. 2010).

In order to fit the spherical surface or curved boundary in numerical simulations, several techniques have been suggested by numerical modelers. To list a few, the cut-cell method can be used, but the presence of degenerate cells or very small cells may become a major difficulty in the application of the cut-cell method (Ingram et al. 2003; Colella et al. 2006; Kleimann et al. 2009). The polyhedron-splitting method can also well generate spherical surface fitting grids (Feng et al. 2007; Nakamizo et al. 2009). An overlapping structured grid, such as the Yin–Yang overset grid in geoscience simulations (Kageyama & Sato 2004; Yoshida & Kageyama 2004) and the six-component grid system in solar wind MHD modeling (Feng et al. 2010), has been used in the computation of spherical shell geometry. A more general overset or Chimera grid, being one of the most important grid techniques for treating problems with complex geometry, has been proposed (Steger & Benek 1987; Chesshire & Henshaw 1990; Brislawn et al. 1995; Meakin 2000; Henshaw 2009), and has achieved successful application in computational aerodynamics incorporating the complex geometry of an aircraft's body.

The adaptive mesh refinement (AMR) technique, originally proposed by Berger & Oliger (1984) for numerical computation of hyperbolic partial differential equations (PDEs), has seen great success in computational fluid dynamics. An AMR grid can adjust automatically and dynamically according to the physical profiles, providing the required spatial resolution while minimizing memory and storage requirements and CPU time. The use of AMR is extremely beneficial and necessary for problems with disparate spatial and temporal scales. The AMR technique has played an increasingly important role in many aspects of MHD computation problems in plasma physics and astrophysics (MacNeice et al. 2000; Ziegler 2005; Olson 2006; Tóth et al. 2006). The AMR technique is also one efficient way to satisfy the requirement of solar wind MHD simulations which must cover a large enough computational domain (i.e., from the solar surface to 1 AU and beyond) and simultaneously achieve high resolution of interested scale structures, such as current sheets and shock waves. The 3D MHD code BATS-R-US, which takes advantage of the AMR technique, has successfully been used in space environment modeling (e.g., Manchester et al. 2006; Tóth et al. 2006).

Parallel AMR applications are sufficiently complex and costly to develop because they require more complex numerical algorithms and programming than uniform fixed mesh approaches (Hornung et al. 2006), and thus AMR software libraries are expected to mitigate these burdens significantly by providing general AMR functionality. Fortunately, several libraries have been built to provide the underlying grid and data management and parallel communication infrastructure for AMR applications. A list of AMR libraries and application codes that are available for download can be found in Norman (2005). For example, some well-known AMR libraries are provided freely, such as PARAMESH (MacNeice et al. 2000) from NASA Goddard Space Flight Center, Chombo (Colella et al. 2007) from the Lawrence Berkeley National Laboratory, and SAMRAI (Gunney et al. 2006) and OVERTURE (Henshaw & Schwendeman 2008) from the Lawrence Livermore National Laboratory. The increased adoption of AMR techniques is partly driven by the public availability of AMR codes and frameworks (MacNeice et al. 2000; Norman 2005; Olson 2006).

The use of AMR grids in combination with overset grids has been presented for the study of rotorcraft flow fields (e.g., Meakin 2000; Wissink et al. 2010) by dividing the computational domain into near-body and off-body fields constructed with body-fitted overset grids and AMR Cartesian grids. The body-fitted overset grids can achieve high-quality boundary conditions and are embedded into off-body AMR Cartesian grids that can automatically capture solution features and adapt the grids. Henshaw & Schwendeman (2008) and Henshaw (2009) have developed an approach for solving time-dependent PDEs using overlapping grids and AMR in the OVERTURE framework. Helios, a recently developed computational platform targeting rotorcraft aeromechanics simulations, is also based on the principle of hybrid grids, using unstructured body-fitted grids near the body surface and AMR grids away from the surface (Sitaraman et al. 2010; Wissink et al. 2010; Strawn 2010; Sankaran et al. 2011).

Motivated by the above considerations, we decompose the spherical shell domain from the Sun to Earth or beyond into near-Sun and off-Sun domains. The Yin–Yang overset grid (Kageyama & Sato 2004; Yoshida & Kageyama 2004) and AMR grid are employed, respectively, in the near-Sun domain and off-Sun domain. The near-Sun Yin–Yang grid can avoid the polar singularity and polar region grid convergence problems and its body-fitting property wins high-quality resolution near the solar surface. The Yin–Yang grid extends only a short distance away from the Sun and the majority of the computational domain is covered with a Cartesian AMR grid that can automatically capture the main features of MHD flows and simultaneously save significant computational resources in comparison with the use of the uniform structured Cartesian grid. The implementation of the AMR computation and parallelization of the off-Sun domain is realized with the help of the AMR package PARAMESH that provides the underlying grid and data management and parallel communication infrastructures (MacNeice et al. 2000; Olson 2006).

The near-Sun part is solved with the space-time conservation element and solution element (CESE) method and the off-Sun part is solved by using a second-order Godunov-type finite-volume scheme with a Harten–Lax–Leer (HLL) approximate Riemann solver for numerical flux. Hereafter, we refer to them as the Yin–Yang–CESE solver and AMR–HLL solver, which are coupled through proper interpolation with timely update and boundary exchange. A domain connectivity module is designed in Section 3.3 to manage the data communications between the near-Sun/off-Sun solvers in the Yin–Yang/AMR overlapping grid systems.

To validate the hybrid 3D solar wind model of the CESE+HLL method, we choose the observed photospheric magnetic field for Carrington rotation (CR) 2069 as initial magnetic input to simulate the ambient solar wind. The comparison of numerical results with observations, such as Mauna Loa Solar Observatory Mark IV (MLSO/MK4) and *Solar and Heliospheric Observatory* (*SOHO*), *Ulysses*, and OMNI data, gives a favorable agreement during this period.

The remainder of this paper is structured as follows. In Section 2, a general description of the MHD solar wind model is presented. Section 3 describes the hybrid grid systems, including the Yin–Yang grid, the AMR grid, and the coupling of the two grid systems. In Section 4, the MHD solvers for the two grid systems are given. The simulation results are given in Section 5. Finally, Section 6 is reserved for summary and discussion.

2. GOVERNING EQUATIONS

The solar wind evolution is governed by modified MHD equations. By splitting the magnetic field (e.g., Tanaka 1994; Gombosi et al. 2003; Nakamizo et al. 2009; Feng et al. 2010), the MHD equations are written as follows:

$$\frac{\partial \rho}{\partial t} + \nabla \cdot \rho \mathbf{u} = 0 \tag{1}$$

$$\begin{aligned}\frac{\partial \rho \mathbf{u}}{\partial t} &+ \nabla \cdot \Big[\rho \mathbf{u}\mathbf{u} + \mathbf{I}\left(p + \frac{1}{2}\mathbf{B}_1^2 + \mathbf{B}_1 \cdot \mathbf{B}_0\right) - \mathbf{B}_1\mathbf{B}_1 \\ &- \mathbf{B}_1\mathbf{B}_0 - \mathbf{B}_0\mathbf{B}_1\Big] = \mathbf{j}_0 \times \mathbf{B}_0 + \rho\left[\mathbf{g} - \boldsymbol{\Omega} \times (\boldsymbol{\Omega} \times \mathbf{r})\right] \\ &- 2\rho\boldsymbol{\Omega} \times \mathbf{u} - \mathbf{B}(\nabla \cdot \mathbf{B})\end{aligned} \tag{2}$$

$$\begin{aligned}\frac{\partial e_1}{\partial t} &+ \nabla \cdot \left[\mathbf{u}\left(e_1 + p + \frac{1}{2}\mathbf{B}_1^2 + \mathbf{B}_1 \cdot \mathbf{B}_0\right) - (\mathbf{u} \cdot \mathbf{B}_1)(\mathbf{B}_1 + \mathbf{B}_0)\right] \\ &= -\mathbf{B}_1 \cdot \frac{\partial \mathbf{B}_0}{\partial t} + \mathbf{E} \cdot \mathbf{j}_0 + \rho\mathbf{u} \cdot \left[\mathbf{g} - \boldsymbol{\Omega} \times (\boldsymbol{\Omega} \times \mathbf{r})\right] \\ &+ Q_e - \mathbf{u} \cdot \mathbf{B}(\nabla \cdot \mathbf{B})\end{aligned} \tag{3}$$

$$\frac{\partial \mathbf{B}_1}{\partial t} + \nabla \cdot (\mathbf{u}\mathbf{B} - \mathbf{B}\mathbf{u}) = -\frac{\partial \mathbf{B}_0}{\partial t} - \mathbf{u}(\nabla \cdot \mathbf{B}) + \eta\nabla(\nabla \cdot \mathbf{B}), \tag{4}$$

where

$$\mathbf{E} = \mathbf{u} \times \mathbf{B}, \quad \mathbf{j}_0 = \nabla \times \mathbf{B}_0$$

and

$$e_1 = \frac{1}{2}\rho\mathbf{u}^2 + \frac{p}{\gamma - 1} + \frac{1}{2}\mathbf{B}_1^2,$$

which corresponds to the modified total energy density consisting of the kinetic energy density, thermal energy density, and magnetic energy density written in terms of $\mathbf{B}_1$.

Here, ρ is the mass density; $\mathbf{u} = (u, v, w)$ are the velocities in the x-, y-, and z-directions; p is the thermal pressure; $\mathbf{B}$, $\mathbf{B}_0$, and $\mathbf{B}_1$ denote the total magnetic field, the potential magnetic field, and its perturbed component such that $\mathbf{B} = \mathbf{B}_0 + \mathbf{B}_1$; t and $\mathbf{r}$ are time and the position vector originating at the center of the Sun; $\mathbf{g} = -GM/r^3 \cdot \mathbf{r}$ is the solar gravitational force; $\mathbf{\Omega}$ is the angular velocity of solar rotation; and γ is the ratio of specific heats. For γ, we use 1.57. Q_e stands for the energy-source term, which is assumed to be responsible for heating and acceleration of the solar wind.

The primitive variables $\rho, \mathbf{v}, p, \mathbf{B}, r, t, \mathbf{g}$ in these equations are normalized by the characteristic values ρ_S, a_S, $\rho_S a_S^2$, $\sqrt{\rho_S a_S^2}$, R_S, R_S/a_S, and a_S^2/R_S, where ρ_S and a_S are the density and ion-acoustic wave speed at the solar surface. Solar rotation is considered in the present study with angular velocity $|\mathbf{\Omega}| = 2\pi/26$ radian day^{-1} (normalized by a_S/R_S in simulations). A factor of $1/\sqrt{\mu}$ has been absorbed into the definition of $\mathbf{B}$. Because $\mathbf{B}_0$ is constant in time and force free, many terms near $\mathbf{B}_0$ in the right-hand side of the equations can vanish. It should be noted that the equations return to the original non-splitting form when $\mathbf{B}_0 = 0$.

In order to reflect the magnetic field topology in the heating and acceleration of solar wind (Nakamizo et al. 2009; Feng et al. 2010), following Feng et al. (2010) the energy-source term Q_e is given as follows:

$$Q_e = Q_1 \exp(-R/L_{Q_1}) + Q_2(R-1)\exp(-R/L_{Q_2}),$$

where $Q_2 = Q_0 C_a$ and $C_a = C_a'/\max(\mathrm{C_a'})$ with $C_a' = \frac{(5.8-1.6e^{[1-(\theta_b/8.5)^3]})^{3.5}}{(1+f_S)^{2/7}}$. Q_1 and Q_0 in this paper are given as 0.8×10^{-9} Jm^{-3} s^{-1} and 6.5×10^{-8} Jm^{-3} s^{-1}, respectively. $R = r/R_S$ is the heliocentric distance. L_{Q_1} and L_{Q_2} are set to be 1 and 0.8. f_S is the magnetic expansion factor which reads $f_S = (\frac{1}{R})^2 \frac{B_{Rs}}{B_R}$ where B_{Rs} and B_R are the magnetic field strength at the solar surface and at the heliocentric distance R. θ_b is the minimum angular separation between an open magnetic field footpoint and its nearest coronal hole boundary. The factor C_a' has been used formerly (Arge et al. 2003; Owens et al. 2008) to empirically study the solar wind.

In order to reduce the numerical error of $\nabla \cdot \mathbf{B}$, the eight-wave scheme (Powell et al. 1999; Groth et al. 2000) and the diffusion control approach of $\nabla \cdot \mathbf{B}$ (Dedner et al. 2002; van der Holst & Keppens 2007; Mignone & Tzeferacos 2010) are employed by adding the source terms $-\nabla \cdot \mathbf{B}(0, \mathbf{B}, \mathbf{u} \cdot \mathbf{B}, \mathbf{u})$ and $\eta\nabla(\nabla \cdot \mathbf{B})$, where η is an artificial diffusion parameter chosen to maximize the diffusion without introducing a numerical instability. In our computation, we use $\eta = C_d(\frac{1}{\Delta x^2} + \frac{1}{\Delta y^2} + \frac{1}{\Delta z^2})^{-1}$, where Δx, Δy, and Δz are grid spacings in Cartesian coordinates and should be replaced by Δr, $r\Delta\theta$, and $r\sin(\theta)\Delta\phi$ in spherical coordinates. Here, $0 \leqslant C_d \leqslant 2$ and we set $C_d = 1.3$. We use heliographic coordinates corotating with the Sun as our reference frame and the solar wind evolution is calculated in Cartesian coordinates associated with the heliographic coordinates.

3. HYBRID GRID SYSTEM

This section describes the Yin–Yang grid for the near-Sun part and the AMR grid for the off-Sun part of the whole computational domain from the Sun to Earth or beyond.

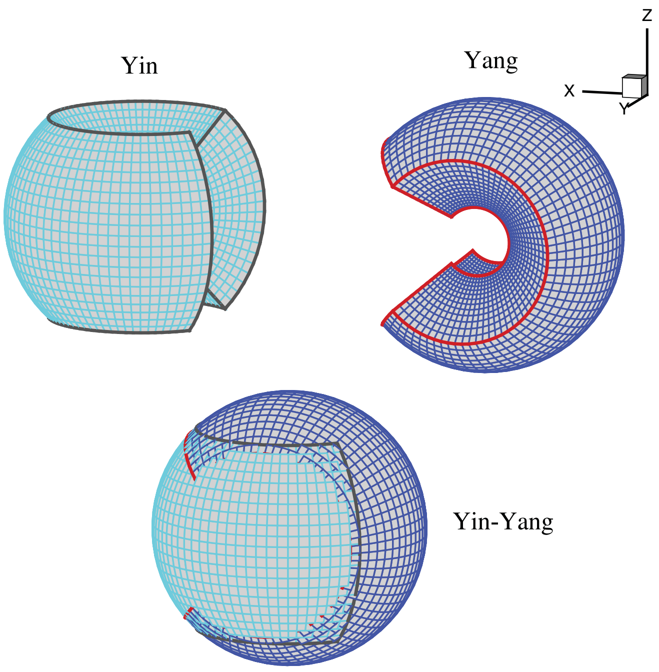

Figure 1. Yin–Yang overset grid.

3.1. Yin–Yang Grid

The Yin–Yang grid (Kageyama & Sato 2004; Yoshida & Kageyama 2004) is composed of two identical component grids combined in a complementary way to cover a spherical surface with partial overlap on their boundaries as shown in Figure 1. Each component grid is a low-latitude spherical mesh, which is defined in the spherical coordinates by

$$\left(\frac{\pi}{4} - \delta \leqslant \theta \leqslant \frac{3\pi}{4} + \delta\right) \cap \left(\frac{\pi}{4} - \delta \leqslant \phi \leqslant \frac{7\pi}{4} + \delta\right),$$

where δ is proportionally dependent on the grid spacing entailed for the minimum overlapping area. The two component grids have the same shape and size and are called "Yin" and "Yang," respectively, after the symbol for the yin and yang of the Chinese philosophy of complementarity, according to Kageyama & Sato (2004) and Yoshida & Kageyama (2004). They are the low-latitude part of the latitude–longitude grid with quasi-uniform grid spacing and polar grid convergence and are singularity-free. The transformation of coordinates and vector components between the Yin and Yang components is straightforward and symmetric, thus allowing for an easy and direct implementation of the grid into a 3D code already employing spherical polar coordinates. The Yin–Yang grid has been successfully employed in the field of geophysical science for simulations of mantle convection and the geodynamo (Kageyama & Sato 2004; Yoshida & Kageyama 2004; Kameyama et al. 2008; Kageyama et al. 2008), atmospheric general-circulation models (Peng et al. 2006), and 3D self-gravitating flows (Wongwathanarat et al. 2010). Here, for the first time, we explore the application of the Yin–Yang grid to the numerical study of solar wind MHD simulations. For our purposes, we define the Yin grid in Figure 1 as being consistent with our physical coordinates. The relation between the Yin coordinates and the Yang coordinates in the Cartesian coordinate system is $(x^e, y^e, z^e) = (-x^n, z^n, y^n)$, where (x^e, y^e, z^e) are the Yin Cartesian coordinates and (x^n, y^n, z^n) are the Yang coordinates. It should be noted that the transformations between the Yin and Yang coordinates are symmetric.

We define mesh points on the Yin and Yang grids as

$$\theta_j = \theta_{\min} + j\Delta\theta,\ j = 0, 1, \ldots, N_\theta + 1$$

$$\phi_k = \phi_{\min} + k\Delta\phi,\ k = 0, 1, \ldots, N_\phi + 1$$

and

$$\Delta\theta = (\theta_{\max} - \theta_{\min})/(N_\theta - 1)$$

$$\Delta\phi = (\phi_{\max} - \phi_{\min})/(N_\phi - 1),$$

where N_θ and N_ϕ are the mesh numbers of the latitude and longitude, respectively. $\theta_{\min} = \frac{\pi}{4}$, $\theta_{\max} = \frac{3\pi}{4}$, $\phi_{\min} = \frac{\pi}{4}$, $\phi_{\max} = \frac{7\pi}{4}$. It is straightforward to construct the 3D Yin–Yang grid for spherical shell geometry by piling up the basic two-dimensional Yin–Yang grids in radial direction, as shown in Figure 1. In this paper, we use $N_\theta = 61$ and $N_\phi = 181$. In the radial direction, we set $r(1) = 1\,R_S$, $r(i+1) = r(i) + \Delta r(i)$, where $i = 1, \ldots, N_r$ ($N_r = 66$ in the present paper). Here, $\Delta r(i) = 0.01 R_S$ if $r(i) < 1.1\,R_S$; $\Delta r(i) = \min(A \times \lg(r(i-1)), \Delta\theta \times r(i-1))$ with $A = 0.01/\lg(1.09)$ if $r(i) < 3.5\,R_S$; and $\Delta r(i) = \Delta\theta \times r(i-1)$ if $3.5 R_S \leqslant r(i) \leqslant 7.0 R_S$. We set $\delta = \Delta\theta$ such that the overlapping region between the Yin–Yang component grids spans $2\Delta\theta$.

For the horizontal (θ, ϕ) boundary or internal border between the Yin and Yang components, according to the general overset technique (Chesshire & Henshaw 1990; Tang et al. 2003), bicubic spline interpolations are applied on the boundary of the Yin and Yang grids to set the horizontal boundary values, as similarly done for the six-component grid by Feng et al. (2010). No boundary conditions in the sphere or angular directions are needed in the Yin–Yang grid. Each grid component communicates with its neighboring component using information from ghost zones derived by interpolation of data between internal grid zones of the neighboring grid component. Interpolation is only required in the two angular coordinates as the radial part of the Yin–Yang grid is identical to that of a spherical polar grid. Then, the interpolated values must be transformed from Yin to Yang grid coordinates and vice versa. It should be noted that the mapping of vector quantities between the Yin grid and Yang grid components is

$$\mathbf{U}(\mathbf{e}) = \begin{pmatrix} 0 & 0 & 1 \\ 0 & 1 & 0 \\ -1 & 0 & 0 \end{pmatrix} \mathbf{U}(\mathbf{n}),$$

where $\mathbf{U}(\mathbf{e})$ and $\mathbf{U}(\mathbf{n})$ denote velocity and magnetic field vectors in Yin and Yang coordinates, respectively.

The outer boundary of the Yin–Yang grid is updated by receiving interpolation data from the off-Sun Cartesian AMR grids and is handled by the domain connectivity module given in Section 3.3.

3.2. The AMR Grid

The off-Sun Cartesian AMR grid is based on the parallel AMR software PARAMESH (MacNeice et al. 2000; Olson 2006), which manages the grid generation, the inter-processor communication, the refinement and de-refinement mechanism, as well as the load balance. A detailed description of PARAMESH can be found on the Web site http://www.physics.drexel.edu/∼olson/paramesh-doc/Users_manual/amr_users_guide.html.

In the AMR part, the computational domain is covered with a hierarchy of blocks distributed among the processors. Each of the blocks is self-similar (i.e., the same numbers of mesh points are in each dimension, the aspect ratios are the same, etc.). Each block is surrounded by two layers of guard cells which are filled either by exchanging data from sibling meshes at the same level or by interpolation from coarse to fine meshes. After guard-filling, each block can be seen as an independent computational element in which an MHD solver can be implemented. Flux conservation at interfaces of different refinement levels is imposed by replacing the flux computed at the coarser level of refinement with the appropriate sum of fluxes at the finer level.

The refinement and de-refinement of a block are controlled by error estimates, the choice of which is an important topic in AMR. There are many kinds of adaptation criteria (Dezeeuw & Powell 1993; Powell et al. 1999; Groth et al. 2000). In this work, we choose a set of criteria based on MHD quantities that can efficiently detect distinctive features of MHD simulations (Linde 1998; Jiang et al. 2010). The refinement criteria are defined as a combination of curl and divergence of velocity and curl of magnetic field, which can respectively capture and resolve shock waves, shear layers, and electric current surfaces:

$$\chi_1 = \sqrt{V}\frac{|\nabla \cdot \mathbf{v}|}{|\mathbf{v}| + \epsilon a} \quad \chi_2 = \sqrt{V}\frac{|\nabla \times \mathbf{v}|}{|\mathbf{v}| + \epsilon a} \quad \chi_3 = \sqrt{V}\frac{|\nabla \times \mathbf{B}|}{|\mathbf{B}| + \epsilon\sqrt{p}}, \tag{5}$$

where a is the plasma sound speed and p is the thermal pressure. The factor $\epsilon \ll 1$ is introduced into Equation (5) to keep them well functioned when either $|\mathbf{v}|$ or $|\mathbf{B}|$ is equal to zero. The factor $\sqrt{V}$ is the length of the cell to the power of 3/2.

If any of the maxima of these criteria in one block is greater than the threshold for refinement, this block is flagged to be refined, while if all of the maxima of these criteria in one block are less than the threshold for coarsening, this block is flagged to be coarsened. The standard deviations near zero for χ_i $_{(i=1,2,3)}$ are computed as

$$\sigma_i = \sqrt{\frac{\sum_{j=1}^{N} \chi_i^2}{N}}, \tag{6}$$

with j visiting all the cells in the computation domain. Then the thresholds for criteria of refinement and definement are given by multiplying each σ_i with properly chosen factors.

3.3. The Domain Connectivity Module

The Yin–Yang grid and the AMR grid are coupled by a parallel domain connectivity module, which is achieved by using message passage interface (MPI). As in the study of rotorcraft flow fields (Sitaraman et al. 2010; Wissink et al. 2010; Sankaran et al. 2011), a domain connectivity module is designed to transfer solution information between the near- and off-Sun solvers. The main tasks of the domain connectivity module include grid hole cutting to remove points unused in the AMR grid, searching the inter-grid boundary points (IGBPs) that need to exchange boundary information through interpolations, and performing the actual interpolation and inter-processor exchange of solution data between the Yin–Yang–CESE solver and the AMR–HLL solver.

Our whole computational domain is a cube region with a size of $[-250\,R_S, 250\,R_S]^3$, centering around the Sun. Initially, the AMR grid is composed of 95,000 blocks with 5–9 levels and each of the blocks has $6 \times 6 \times 6$ meshes. The blocks become

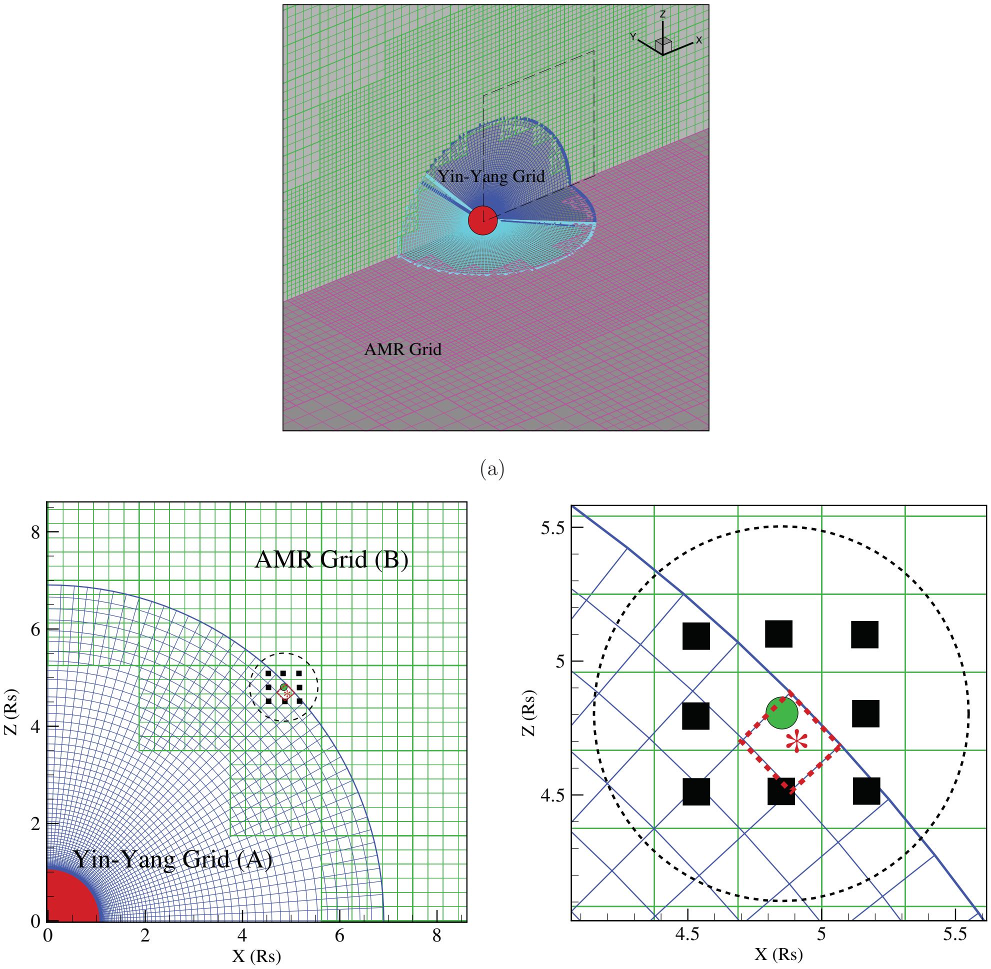

(a)

(b)

(c)

Figure 2. (a) Hole cutting of the AMR grid and 3D representation of the Yin–Yang/AMR overlapping grid systems; (b and c) the donor–receptor cells method.

small when they are close to the Sun surface. The Yin–Yang grid is embedded in the background AMR Cartesian grid and extends from 1.0 R_S to 7.0 R_S in the radial direction.

The coupling of the Yin–Yang/AMR grids is shown in Figure 2(a). The two grid systems overlap within a spherical shell from 6.0 R_S to 7.0 R_S, where data are exchanged. In order to maintain a smooth transition of the solution variables from the near-Sun to off-Sun parts, the grids in the overlapping regions should have comparable grid resolutions. Therefore, the AMR blocks in the overlapping regions are refined until they reach the grid resolutions of the outer boundary points of Yin–Yang grid system.

At the beginning of the simulation, the domain connectivity module does the searching and flagging of near-Sun/off-Sun IGBPs. For the Yin–Yang grid system, the IGBPs are the outer boundary points. For AMR grid system, the IGBPs are the nearest two layers of points neighboring the interior of the sphere surface at 6.0 R_S.

The IGBPs are not used to advance the solution but to receive solution values interpolated from their overlapping grids. We use a dual-way coupling method between the Yin–Yang and AMR grid systems; that is, we need to obtain the data of IGBPs for both of them by interpolation from each other.

We apply the Lagrange interpolation to perform the data interpolation in the Yin–Yang/AMR overlapping grids. As in Chiu & Meakin (1995) and Cai et al. (2006), the concept of donor and receptor points is used, as shown in Figures 2(b) and (c). The Yin–Yang Grid (A) and the AMR Grid (B) overlap with each other. A cell-centered receptor point, say on Grid A (marked by the red star), needs to receive solution information from Grid B to provide the boundary condition for Grid A. The donor cell for this receptor point is identified as the cell on Grid B that contains the receptor point. (We mark this donor cell with the green bold point in Figure 2(c).)

The points (marked by black solid square symbols) surrounding the donor cell form the set of interpolation stencil points for the receptor point. The solution variables at the receptor points can then be easily obtained by using the Lagrange interpolation over this set of stencil points. In the present paper, we use 27 stencil points for interpolation in three dimensions, so that the Lagrange interpolation has third-order accuracy. As the numerical test will show, this kind of interpolation for the boundary data determination in the Yin–Yang/AMR overlapping grids does not degrade the numerical accuracy of the whole model.

The domain connectivity module also needs to account for the specific transformations of vector fields and coordinates between the Yang and AMR grid systems. That is to say, if grid A is the Yang grid, the coordinates of the receptor point should be transformed to the Yin coordinates (i.e., the physical coordinates) when searching its corresponding donor point on Grid B. After the interpolation, transformations are also needed for vectors of velocity and magnetic field to obtain the correct values at the original point of grid A and vice versa.

4. MHD SOLVERS AND TIME STEPPING

Our hybrid model consists of two different MHD solvers: the CESE method on the Yin–Yang grid in the near-Sun region and the HLL method on the AMR grid in the off-Sun region, in order to solve the MHD solar wind governing Equations (1)–(4). The details of these two numerical algorithms for the MHD equations can be referred to Kurganov et al. (2001), Ziegler (2005), and Feng et al. (2007, 2010). Here, in order to show how these two solvers cooperatively work to advance the solution, only the main features of the numerical solvers are described briefly.

4.1. MHD Solvers

The SIP-CESE MHD model (Feng et al. 2007, 2010) is implemented on the Yin–Yang grid system. The numerical improvements of the SIP-CESE MHD model, such as the courant-number insensitive method, multiple time step method, and fast multi-grid Poisson solver for cleaning magnetic field divergence, have been provided in detail by Feng et al. (2010).

On the off-Sun AMR grid system, the finite-volume MHD solver of second-order accuracy is applied, where the MHD equations are solved with a cell-centered Godunov-type finite-volume scheme (Kurganov et al. 2001; Ziegler 2005) for spatial discretization, in conjunction with second-order Monotone Upstream Schemes for Conservation Laws method for reconstruction and with approximate Riemann solvers of HLL for numerical fluxes (Harten et al. 1983). For time integration, the explicit second-order Runge–Kutta time stepping is used.

It should be mentioned that the splitting of magnetic field $\mathbf{B}$ into time-dependent part $\mathbf{B}_1$ and time-independent part $\mathbf{B}_0$ is very important for solving the MHD equations in a (near) conservation form, since the total energy density can be completely dominated by the magnetic energy $\mathbf{B}_0^2/2$ near the Sun, which can lead to negative pressure if calculated from the total energy density. This problem can be mitigated, particularly near the Sun, by splitting, and for small plasma β regions, solving for the deviation $\mathbf{B}_1$ from the embedded field $\mathbf{B}_0$ is inherently more accurate than solving for the full magnetic field vector $\mathbf{B}$. Thus, the splitting form of the MHD solar wind governing Equations (1)–(4) is used in the CESE solver on the near-Sun grid system while the original non-splitting form is taken in the HLL solver on the off-Sun AMR grid system.

4.2. Time Stepping

The iterative time steps determined by the Courant-Friedrichs-Lewy (CFL) stability conditions differ by about 10–20 times between the Yin–Yang and AMR grid systems. The same time stepping strategy in the entire computational domain decreases the numerical performance and wastes computational resource. Thus, in the simulation we use multiple time stepping methods (van der Ven et al. 1997; Maurits et al. 1998) for the two grid systems. The use of a multiple time stepping algorithm between the Yin–Yang and AMR grid systems can speed up the computation.

The implementation of this multiple time stepping algorithm on the hybrid grid systems is designed as follows. First, we calculate the usual time step $\Delta t1$ and $\Delta t2$ for the Yin–Yang and AMR grids, respectively, by using the CFL stability condition with the Courant number 0.8. Then we further constrain the time step as, $\Delta t2 = M \times \Delta t1$, $M = \mathrm{int}(\Delta t2/\Delta t1)$, where "int($x$)" means the integer part of x playing the same role as that of the FORTRAN intrinsic function. When the solution in the AMR grid advances a single step of $\Delta t2$, the solution in the Yin–Yang grid needs to advance M time steps of $\Delta t1$ in order to arrive at the same time level with the AMR grid. Then after each synchronization step, $\Delta t1$ and $\Delta t2$ are determined again. At the same time level, the boundary values of the Yin–Yang and AMR grids are obtained by interpolations from each other with the help of the domain connectivity module as described in Section 3.3. Otherwise, the values of the Yin–Yang grid's outer boundary are calculated by $U_1(t + i \times \Delta t1) = U_2(t) + i \times \Delta t1 \times U_{2t}(t)$, where $i = 1, \ldots, M - 1$ and $U_2(t)$, $U_{2t}(t)$ stand for the values of U and their time derivative at t on the AMR grid system. Then these boundary values of U_1 at $M - 1$ time step levels are all packaged into buffers and are transferred to the Yin–Yang grid system, which is also completed by the domain connectivity module.

5. NUMERICAL RESULTS FOR THE STEADY SOLAR WIND OF CR 2069

In order to validate the newly established hybrid solar wind model, we present a numerical simulation for the steady solar wind of CR 2069. In the simulation, the boundary conditions at both the bottom and the outmost surfaces of the computational domain are prescribed in the same way as done by Feng et al. (2010), where the time-dependent inner boundary condition with mass flux limitation by a *Ulysses* observation is employed according to Hayashi (2005). The temperature and density are set to be 1.3×10^6 K and 1.0×10^8 cm^{-3}, respectively. The initial state throughout the domain is determined by the analytic spherical symmetric Parker solar wind solution and the potential magnetic field model based on the synoptic map of the line-of-sight photospheric magnetograms for CR 2069 from the Wilcox Solar Observatory. Then the governing equations are advanced by using the hybrid model above until a steady state is achieved.

Figure 3 compares the MHD solution and the observations on the surfaces of both $r = 1.15\ R_s$ (a, b) and $r = 2.5\ R_s$ (c, d). Figures 3(a) and (b) are the synoptic maps of the simulated mass flux density and the full-disk observations of the Extreme ultraviolet Image Telescope (EIT) aboard the spacecraft of *SOHO* on the surface of $r = 1.15\ R_s$. Figure 3(c) superimposes the plasma density isolines on the contour map of the radial velocity at $r = 2.5\ R_s$ and Figure 3(d) presents the synthesized white-light polarized brightness (pB) image at the west limb constructed from the successive images centered at $r = 2.5\ R_s$ from the LASCO C2.

The most prominent features in Figure 3 are the large equatorial extensions of the southern polar coronal hole (PCH) and the isolated equatorial holes (IEHs), which are characterized by the low-latitude presence of relatively low density, high mass flux density, and low-latitude boundaries between the open and closed magnetic field regions in Figure 3(a) and the dark areas of the EIT observation in Figure 3(b). Both the numerical result and the EIT observation at $r = 1.15\ R_s$ demonstrate that there are isolated holes around $(\theta, \phi) = (0^\circ, 280^\circ)$ and $(-30^\circ, 200^\circ)$ and that the southern extending PCH can reach $\theta = -30^\circ$ around $\phi = 150^\circ$. Additionally, the isolated equatorial coronal holes and the southern extending PCH can be further confirmed by the distribution of the bright structures in the pB observation from LASCO C2 and the numerical results at $r = 2.5\ R_s$.

Another characteristic is the warp structure of the magnetic neutral line (MNL) between $\phi = 200^\circ$ and $\phi = 330^\circ$ in Figure 3(c), which is associated with the IEH and the equatorial extension of the southern PCH. The southernmost point of the MNL extends to $\theta = -30^\circ$ and the northernmost point to $\theta = 10^\circ$. The bright structures in Figure 3(d) also suggest the

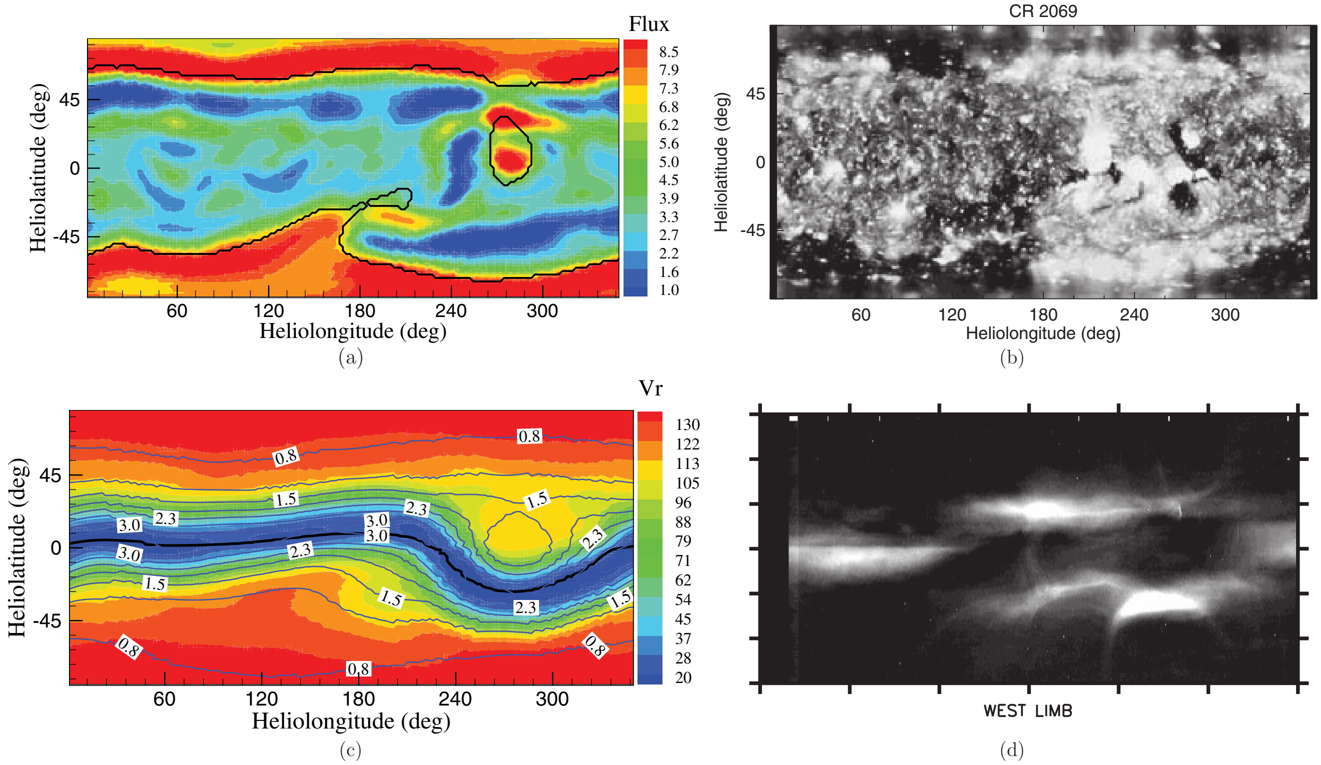

Figure 3. Synoptic maps of the simulated mass flux density (a) in units of 10^{13} cm^{-2} s^{-1} and full-disk observations from *SOHO*/EIT (b) on the surface of $r = 1.15\ R_s$. The solid lines in (a) denote the boundaries between the open and closed magnetic field areas. The isolines (solid lines) of proton number density in units of cm^{-3} are superimposed on the contour map of the radial velocity in units of km s^{-1} (c) and the synthesized white-light polarized brightness (pB) image (d) observed by LASCO/C2 images centered at $r = 2.5\ R_s$.

relatively large poleward extensions of the streamer of the closed magnetic field around the two locations. Generally speaking, the MNL is often flat during solar minima (Hoeksema et al. 1983; Gibson et al. 2009). However, Wang et al. (2009) found that it was the weaker solar polar fields that led to a lot of peculiarities during the 2008 solar minimum, which included large warps of the heliospheric current sheets (HCSs).

Figures 4(a) and (b) exhibit the pB observations from 1.15 R_s to 6 R_s on April 21 and May 13, where the observations from 1.15 R_s to 2.3 R_s are adopted from MLSO/MK4 white-light observation and the outer fields of view from 2.3 R_s to 6 R_s are from LASCO C2 observations. Figures 4(c) and (d) present the synthesized pB images from the simulation on the meridional planes at $\phi = 180°–0°$ (c) and $\phi = 270°–90°$ (d) from 1.15 R_s to 6.0 R_s, in which we enhance the images inside and outside 2.3 R_s separately. Figures 4(e) and (f) are the magnetic field topologies projected on the same meridional planes as in (c) and (d). It should be noted that the results on the meridional planes at $\phi = 180°–0°$ and $\phi = 270°–90°$ roughly correspond to the observations on April 21 and May 13, respectively.

Figure 4 shows that the locations of the bright structures at both limbs from the simulation results are in good agreement with those observed by MLSO/MK4 and LASCO C2. Comparing Figures 3 and 4, we can see that the brightest streaks at both limbs in Figures 4(a) and (c) correspond to the helmet streamer, the high-density regions in the neighborhood of the MNL and the high inclined, radially oriented bright structures in the southeast of Figures 4(b) and (d) are identified to be the emission from the area of the tilted MNL discussed in Figure 3 and its underlying streamer. In Figure 4(f), the high-density pseudostreamer structure (Wang et al. 2009) produces the slightly bright rays in the northeast of Figure 4(b) and their counterparts in Figure 4(d).

Figure 5 presents the pseudocolor image of the radial solar wind speed and magnetic field lines in the *X–Z* plane (a), where the black squares represent the blocks of different refinement levels and the white solid lines with arrowheads stand for the magnetic field lines, and radial profiles of the radial velocity (b) and proton number density (c) from 1 to 20 R_s at two locations with different latitudes $\theta = 8°$ (solid line) and $\theta = 79°$ (dashed line) in the *X–Z* plane. From this graph, we can see that low-speed solar wind (>450 km s^{-1}), whose latitudinal width is about 25°, is concentrated on the regions around the MNL and the high-speed solar wind (>700 km s^{-1}) flows mainly in the high- and middle-latitudes (HMLs). In addition, the middle-speed solar wind (450–700 km s^{-1}) even appears at very low latitudes in the left part of Figure 5(a), which corresponds to the extending hole of southern PCH. Figures 5(b) and (c) show that the radial bulk speed changes very slightly and the number density approaches r^{-2} beyond 10 R_s and the profile for low-speed solar wind basically agrees with those derived from observations by Sheeley et al. (1997). The smooth variations of the physical quantities justify our interface module in the Yin–Yang and AMR overlapping domain.

Figure 6 displays the simulated distributions of radial velocity in the meridional plane and in the equatorial plane from about 6 to 215 R_s. Figure 6(a) basically exhibits the bimodal structure of the fast solar wind at coronal holes and the slow solar wind around the low-latitude HCS. The abruptly southward deflection of the low-speed solar wind in the left part of Figure 6(a) results from the warping structure of the HCS. Due to solar rotation, the *X–Z* plane beyond 150 R_s continuously intercepts the

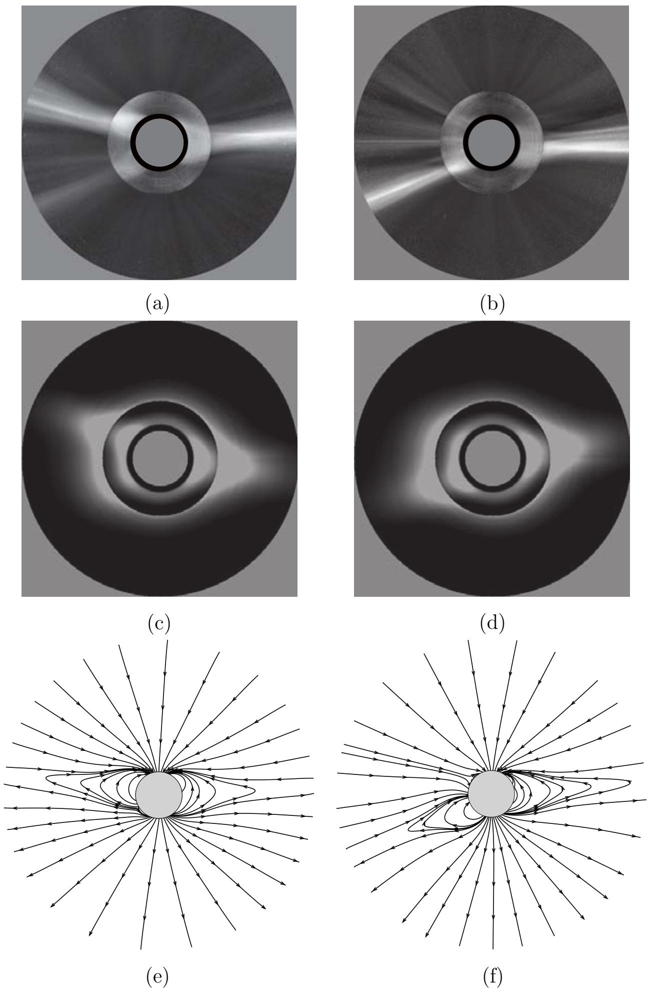

Figure 4. Coronal composite images on April 21 (a) and May 13 (b) and the distribution of the simulated pB on the meridional planes at $\phi = 180°–0°$ (c) and $\phi = 270°–90°$ (d) from 1.15 to 6 R_S. The magnetic field topology projected on the meridional planes at $\phi = 180°–0°$ (e) and $\phi = 270°–90°$ (f) from 1 to 6 R_s, where the innermost solid gray circle denotes the solar disk.

low-speed solar wind around HCS among longitudes from 230° to 280° at 2.5 R_s. Figure 6(b) also depicts the sector structure in the equatorial plane and the middle-speed solar wind flows from the IEH and the extending hole.

Figure 7 displays the comparisons of the MHD results with the daily averaged data obtained by *Ulysses* between latitudes ±80° during its third fast latitudinal scan in 2007, with a heliocentric distance of 1.5–2.5 AU. The *Ulysses* data are scaled to 1 AU by assuming an r^{-2} falloff for B_r and N, an $r^{-2(\gamma-1)}$ ($\gamma = 1.46$) variation for T and no change for V_r, as in Usmanov et al. (2000). It can be seen from Figure 7 that the latitudinal changing trends of the solar wind parameters obtained from MHD results are basically consistent with those from *Ulysses* observations. The hybrid 3D MHD model reproduces fast, tenuous, and hot solar wind at high latitudes and slow, dense, and cold solar wind near the equator. The slopes of velocity and temperature transitions are roughly consistent with *Ulysses* observations. For the simulation, V_r is a little faster and N is a little lower near the polar areas.

Figure 8 compares the simulated results for CR 2069 with OMNI data that combine the measurements from multiple spacecraft near point L1. Obviously, the hybrid MHD model reproduces three observed middle-speed streams and their associated corotating interaction regions, which are characteristic of the enhancements of the plasma density N and temperature T in front of the high-speed streams. The rate of density enhancement and the slope of the rising solar wind speed in the simulation are roughly consistent with those of the observations, although the second simulated middle-speed stream rises late by about 0.5 day and the third one arrives early by about 1.5–2 days. In addition, both Figures 7 and 8 show that the hybrid MHD model captures the polarity of the magnetic field, although the magnitude of the magnetic field is a little lower compared with the observations.

6. SUMMARY AND CONCLUSION

In summary, a hybrid 3D MHD model for solar wind modeling of the Sun to Earth system is proposed, where an innovative dual-mesh grid system consisting of two grid systems is designed with a near-Sun Yin–Yang grid to fit the spherical surface boundary and overcome the well-known coordinate singularity as well as polar grid convergence problems, and with an off-Sun block structured AMR Cartesian grid to automatically capture the far-field plasma flow features. A domain connectivity module is provided to perform the interpolation and transfer of the solution variables between the Yin–Yang/AMR overlapping grid systems.

In the present version of this 3D code, the CESE method is for the first time employed in the Yin–Yang grid of the near-Sun region, while the HLL scheme is used in the AMR grid of the off-Sun region. In this way, grid quality in both the near-Sun and

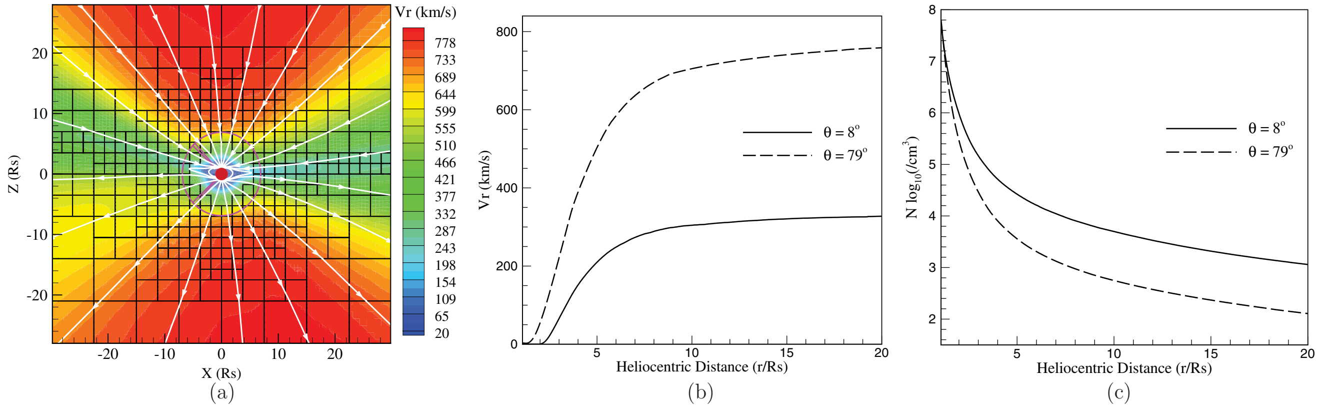

Figure 5. Pseudocolor image of radial solar wind speed V_r and magnetic field (white solid lines with arrowheads) in the X–Z plane (a), in which the black squares represent the blocks of different refinement levels. Radial profiles of radial velocity V_r (b) and number density (c) from 1 to 20 R_s at two locations with different latitudes $\theta = 8°$ (solid line) and $\theta = 79°$ (dashed line) in the X–Z plane.

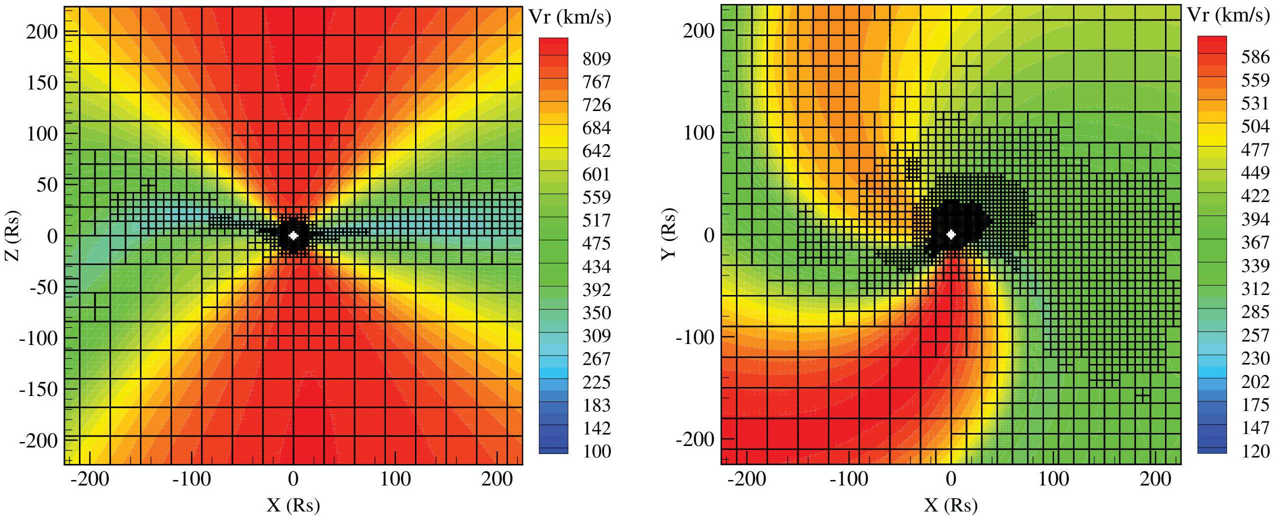

(a) (b)

Figure 6. Contours of radial velocity on the *X*–*Z* plane (a) and on the *X*–*Y* plane (b) in the AMR domain, in which the black squares represent the blocks of different refinement levels.

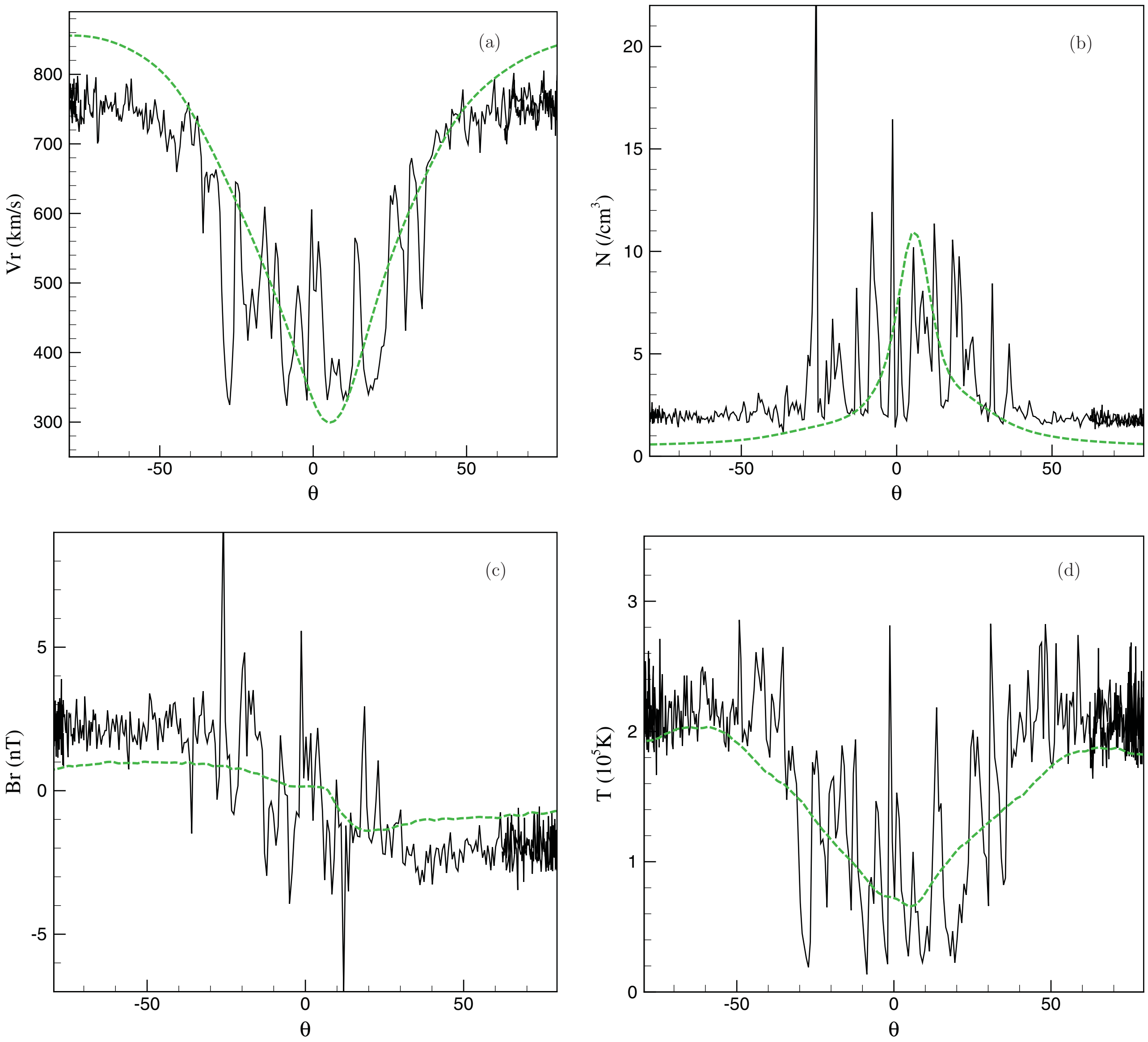

Figure 7. Comparisons of solar wind radial velocity V_r (a), proton number density *N* (b), radial magnetic field B_r (c), and temperature *T* (d) between the MHD results and the daily averaged data recorded by *Ulysses* between latitudes ±80° during its third fast latitudinal scan in 2007.

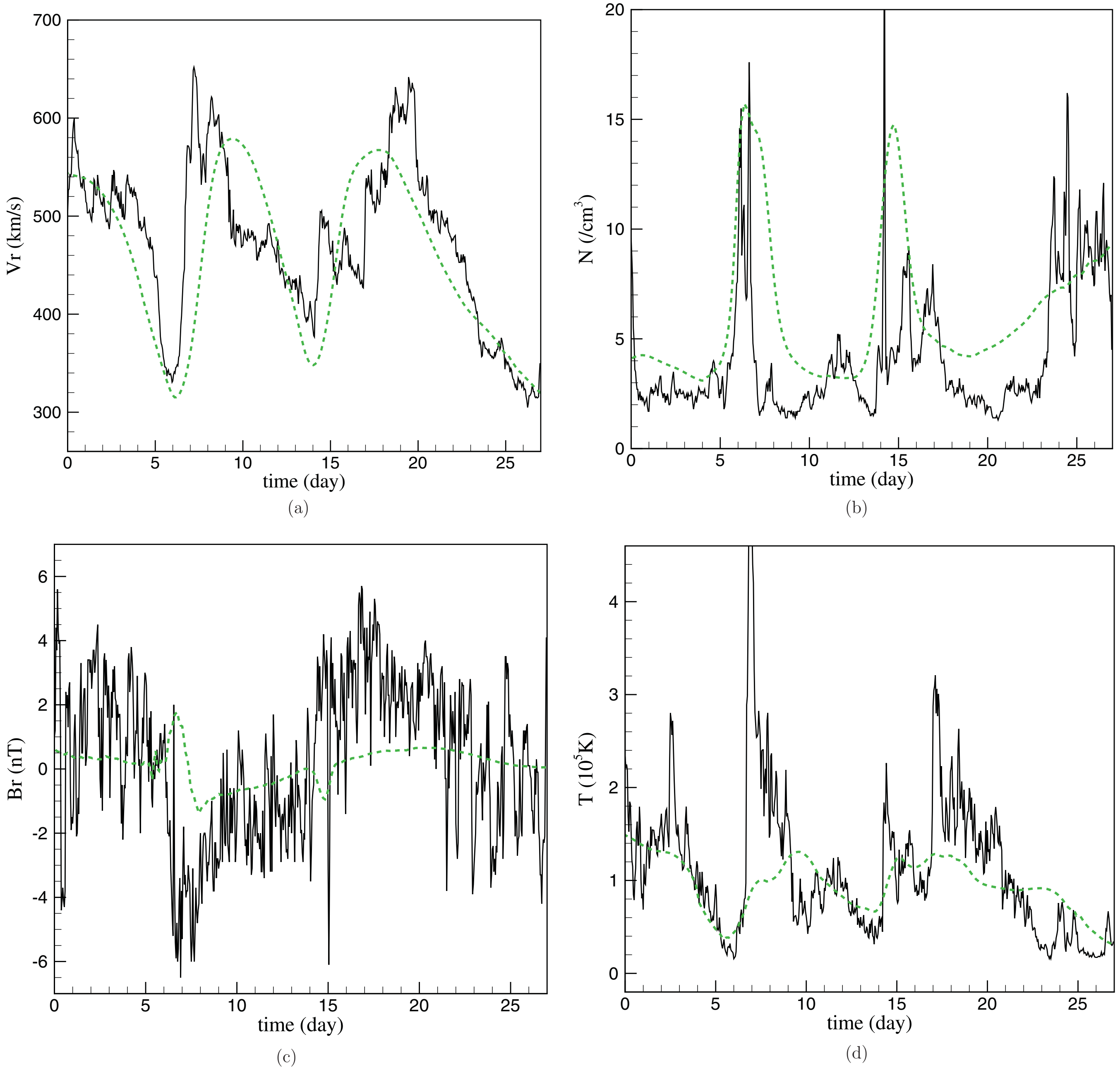

(a)

(b)

(c)

(d)

Figure 8. Comparisons of solar wind radial velocity V_r (a), proton number density N (b), radial magnetic field B_r (c), and temperature T (d) between the MHD results and the 1 hr averaged data from OMNI near 1 AU. The observed data start from 2008 April 16.

off-Sun regions is no longer an issue and adaptive meshing in the off-Sun region is straightforward to implement. At the same time, Cartesian grids are fast and efficient because there are no grid metric terms with structured data layout maximizing cache performance. Also, since Cartesian grids facilitate direct use of high-order numerical methods, we have many viable choices of trying other modern numerical schemes (e.g., Pen et al. 2003; Kleimann et al. 2004, 2009; Yee & Sjögreen 2006, 2007; Toro 2009; Balsara et al. 2009; Mignone & Tzeferacos 2010; Ziegler 2011) in the off-Sun region to develop other versions of this kind of hybrid code for 3D solar wind models.

In the near-Sun region, where plasma β is much smaller, the splitting of magnetic field $\mathbf{B}$ into time-dependent part $\mathbf{B}_1$ and time-independent part $\mathbf{B}_0$ is helpful for positivity maintenance of the thermal pressure. In the off-Sun region, we suggest that the original non-splitting form of magnetic field $\mathbf{B}$ be used. This treatment of the magnetic field can enhance solution accuracy in both the near-Sun and off-Sun regions.

This newly established hybrid 3D MHD model is validated to produce the background solar wind of CR 2069 and compare the numerical results with the observations, such as MLSO/MK4, *SOHO* LASCO/C2, *SOHO*/EIT, *Ulysses*, and OMNI data. The comparisons show that the model captures a lot of peculiarities in the corona in the 2008 solar minimum and basically reproduces the large-scale solar wind structures in interplanetary space. The simulation near the Sun shows the observed large equatorial extensions of the southern PCH and the presence of the IEHs is rarely seen in the previous minima. In addition, the numerical results also yield the warp structure of the MNL between $\phi = 200°$ and $\phi = 330°$ and its associated low-speed solar wind distribution in interplanetary space. Finally, the solar wind parameters from the hybrid 3D

MHD model are roughly consistent with *Ulysses* observations and with the temporal variations from OMNI data combining the measurements by multiple spacecraft near point L1. Of course, some differences between numerical results and observations commonly exist as claimed by Feng et al. (2010).

This work is jointly supported by the National Natural Science Foundation of China (41031066, 40921063, 40874091, 40890162, 40904050, 40874077, 41074121, and 41074122), and the Specialized Research Fund for State Key Laboratories. Dr. S. T. Wu is supported by AFOSR (grant FA9550-07-1-0468), AURA Sub-Award C10569A of NSO's Cooperative Agreement AST 0132798, and NSF (grant ATM-0754378). The numerical calculation has been completed on our SIGMA Cluster computing system. The PARAMESH software used in this work was developed at the NASA Goddard Space Flight Center and Drexel University under NASA's HPCC and ESTO/CT projects and under grant NNG04GP79G from the NASA/AISR project. Wilcox Solar Observatory data used in this study were obtained via the Web site http://wso.stanford.edu. The Wilcox Solar Observatory is currently supported by NASA. The MLSO coronagraphs are operated by the High Altitude Observatory, which is sponsored by the National Science Foundation (USA). *SOHO* is a project of international cooperation between ESA and NASA. The STEREO/SECCHI data are produced by a consortium of NRL (US), LMSAL (US), NASA/GSFC (US), RAL (UK), UBHAM (UK), MPS (Germany), CSL (Belgium), IOTA (France), and IAS (France). We thank the SPDF COHO Web database for helpfully providing data. The OMNI data are obtained from the GSFC/SPDF OMNI Web interface at http://omniweb.gsfc.nasa.gov. The authors express their sincere thanks to the anonymous reviewer for constructive comments.

REFERENCES

Arge, C. N., Odstrcil, D., Pizzo, V. J., & Mayer, L. R. 2003, in AIP Conf. Proc. 679, Solar Wind Ten: Improved Method for Specifying Solar Wind Speed Near the Sun, ed. M. Velli, R. Bruno, & F. Malara (Woodbury, NY: AIP), 190

Balsara, D. S., Rumpf, T., Dumbser, M., & Munz, C.-D. 2009, J. Comput. Phys., 228, 2480

Berger, M. J., & Oliger, J. 1984, J. Comput. Phys., 53, 484

Brislawn, K. D., Brown, D. L., Chesshire, G. S., & Saltzman, J. S. 1995, in ICASE/LaRC Workshop on Adaptive Grid Methods, ed. J. C. South, Jr., J. L. Thomas, & J. Vanrosendale (NASA CP 3166; Hampton, VA: NASA Langley Research Center), 95

Cai, J., Tsai, H. M., & Liu, F. 2006, Comput. Fluids, 35, 1290

Chesshire, G., & Henshaw, W. D. 1990, J. Comput. Phys., 90, 1

Chiu, I., & Meakin, R. 1995, in 33rd Aero. Sci. Mtg. Reno, NV, 1995 (Paper AIAA-95-054; Reston, VA: American Institute of Aeronautics and Astronautics)

Colella, P., Graves, D. T., Keen, B. J., & Modiano, D. 2006, J. Comput. Phys., 211, 347

Colella, P., et al. 2007, Chombo Software Package for AMR Applications, Technical Report, Lawrence Berkeley National Laboratory (http://seesar.lbl.gov/anag/chombo/ChomboDesign-2.0.pdf)

Dedner, A., Kemm, F., Kröner, D., Munz, C., Schnitzer, T., & Wesenberg, M. 2002, J. Comput. Phys., 175, 645

Dezeeuw, D., & Powell, K. G. 1993, J. Comput. Phys., 104, 56

Dryer, M. 2007, Asian J. Phys., 16, 97

Feng, X. S., Xiang, C. Q., & Zhong, D. K. 2011, Sci. Sin-Terrae, 41, 1

Feng, X. S., Yang, L. P., Xiang, C. Q., Wu, S. T., Zhou, Y. F., & Zhong, D. K. 2010, ApJ, 723, 300

Feng, X. S., Zhou, Y., & Wu, S. T. 2007, ApJ, 655, 1110

Gibson, S. E., Kozyra, J. U., de Toma, G., Emery, B. A., Onsager, T., & Thompson, B. J. 2009, J. Geophys. Res., 114, A09105

Gombosi, T., De Zeeuw, D., Powell, K., Ridley, A., Sokolov, I., Stout, Q., & Tóth, G. 2003, in Space Plasma Simulation, ed. J. Büchner, M. Scholer, & C. Dum (Lecture Notes in Physics, Vol. 615; Berlin: Springer), 247

Groth, C. P. T., De Zeeuw, D. L., Gombosi, T. I., & Powell, K. G. 2000, J. Geophys. Res., 105, 25053

Gunney, B. T., Wissink, A. M., & Hysom, D. A. 2006, J. Parallel. Distr. Com., 66, 1419

Harten, A., Lax, P. D., & van Leer, B. 1983, SIAM Rev., 25, 35

Hayashi, K. 2005, ApJS, 161, 480

Henshaw, W. D. 2009, in ASP Conf. Ser. 406, Numerical Modeling of Space Plasma Flows: ASTRONUM-2008, ed. N. V. Pogorelov et al. (San Francisco, CA: ASP), 231

Henshaw, W. D., & Schwendeman, D. W. 2008, J. Comput. Phys., 227, 7469

Hoeksema, J. T., Wilcox, J. M., & Scherrer, P. H. 1983, J. Geophys. Res., 88, 9910

Hornung, R., Wissink, A., & Kohn, S. 2006, Eng. Comput., 22, 181

Ingram, D. M., Causon, D. M., & Mingham, C. G. 2003, Math. Comput. Simul., 61, 561

Jiang, C., Feng, X., Zhang, J., & Zhong, D. 2010, Sol. Phys., 267, 463

Kageyama, A., Miyagoshi, T., & Sato, T. 2008, Nature, 454, 1106

Kageyama, A., & Sato, T. 2004, Geochem. Geophys. Geosyst., 5, 9005

Kameyama, M., Kageyama, A., & Sato, T. 2008, Phys. Earth Planet. Int., 171, 19

Kleimann, J., Kopp, A., Fichtner, H., & Grauer, R. 2009, Ann. Geophys., 27, 989

Kleimann, J., Kopp, A., Fichtner, H., Grauer, R., & Germaschewski, K. 2004, Comput. Phys. Commun., 158, 47

Kurganov, A., Noelle, S., & Petrova, G. 2001, SIAM J. Sci. Comput., 23, 707

Linde, T. J. 1998, PhD thesis, Univ. Michigan

MacNeice, P., Olson, K. M., Mobarry, C., de Fainchtein, R., & Packer, C. 2000, Comput. Phys. Commun., 126, 330

Manchester, W., Ridley, A., Gombosi, T., & DeZeeuw, D. 2006, Adv. Space. Res., 38, 253

Maurits, N. M., van der Ven, H., & Veldman, A. E. P. 1998, Comput. Methods Appl. Mech. Eng., 157, 133

Meakin, R. 2000, Comput. Methods Appl. Mech. Eng., 189, 1077

Mignone, A., & Tzeferacos, P. 2010, J. Comput. Phys., 229, 2117

Nakamizo, A., Tanaka, T., Kubo, Y., Kamei, S., Shimazu, H., & Shinagawa, H. 2009, J. Geophys. Res., 114, 7109

Norman, M. 2005, in Adaptive Mesh Refinement—Theory and Applications, Vol. 41, ed. T. J. Barth et al. (Berlin: Springer), 413

Olson, K. 2006, in Parallel Computational Fluid Dynamics, ed. A. Deane et al. (College Park, MD: Elsevier), 341

Owens, M. J., et al. 2008, Space Weather, 6, S08001

Pen, U.-L., Arras, P., & Wong, S. 2003, ApJS, 149, 447

Peng, X., Xiao, F., & Takahashi, K. 2006, Q. J. R. Meteorol. Soc., 132, 979

Powell, K. G., Roe, P. L., Linde, T. J., Gombosi, T. I., & de Zeeuw, D. L. 1999, J. Comput. Phys., 154, 284

Sankaran, V., et al. 2011, in 49th AIAA Aerospace Sciences Meeting Including the New Horizons Forum and Aerospace Exposition, Orlando, Florida, 2011 January 4–7, (Paper AIAA-2011-1105; Reston, VA: American Institute of Aeronautics and Astronautics)

Sheeley, N. R., et al. 1997, ApJ, 484, 472

Sitaraman, J., Floros, M., Wissink, A., & Potsdam, M. 2010, J. Comput. Phys., 229, 4703

Steger, J. L., & Benek, J. A. 1987, Comput. Methods Appl. Mech. Eng., 64, 301

Strawn, R. 2010, Comput. Sci. Eng., 12, 27

Tanaka, T. 1994, J. Comput. Phys., 111, 381

Tang, H., Casey Jones, S., & Sotiropoulos, F. 2003, J. Comput. Phys., 191, 567

Toro, E. 2009, Riemann Solvers and Numerical Methods for Fluid Dynamics (Berlin: Springer)

Tóth, G., de Zeeuw, D. L., Gombosi, T. I., & Powell, K. G. 2006, J. Comput. Phys., 217, 722

Usmanov, A. V., Goldstein, M. L., Besser, B. P., & Fritzer, J. M. 2000, J. Geophys. Res., 105, 12675

van der Holst, B., & Keppens, R. 2007, J. Comput. Phys., 226, 925

van der Ven, H., Niemann-Tuitman, B. E., & Veldman, A. E. P. 1997, J. Comput. Appl. Math., 82, 423

Wang, Y., Robbrecht, E., & Sheeley, N. R. 2009, ApJ, 707, 1372

Wissink, A., Kamkar, S., Pulliam, T., Sitaraman, J., & Sankaran, V. 2010, in 40th AIAA Fluid Dynamics Conference and Exhibit, Chicago, Illinois, 2010 June 28–July 1 (Paper AIAA-2010-4554; Reston, VA: American Institute of Aeronautics and Astronautics)

Wongwathanarat, A., Hammer, N. J., & Müller, E. 2010, A&A, 514, A48

Yee, H., & Sjögreen, B. 2006, J. Sci. Comput., 29, 115

Yee, H. C., & Sjögreen, B. 2007, J. Comput. Phys., 225, 910

Yoshida, M., & Kageyama, A. 2004, Geophys. Res. Lett., 31, 12609

Ziegler, U. 2005, Comput. Phys. Commun., 170, 153

Ziegler, U. 2011, J. Comput. Phys., 230, 1035